A quick prediction for the transformation of red blood cell morphology with deep learning technique

View Online   Export Citation   CrossMark

Sisi Tan[a] iD

AFFILIATIONS

School of Physics, Changchun University of Science and Technology, Weixing Street 7089, Changchun, Jilin 130022, China

[a]Author to whom correspondence should be addressed: tansisi@cust.edu.cn

ABSTRACT

Red blood cells (RBCs) are essential for maintaining human health, and their morphological abnormalities serve as critical diagnostic indicators for various blood disorders. To predict RBC morphology accurately and efficiently, we develop a deep learning model that solves the inverse problem of inferring RBC shapes from their geometric properties. The model utilizes spherical harmonics to reconstruct the RBC surface, thereby reducing the degrees of freedom and enabling efficient prediction. It is applied to predict the stomatocyte–discocyte–echinocyte (SDE) transformation of RBCs, with results strongly correlating with experimental observations and numerical simulations, thereby validating the model's accuracy. Additionally, the model demonstrates robustness with low sensitivity to structural parameters, such as dataset size and hidden layer depth. Even with a small dataset and shallow hidden layers, it remains effective, with training completed in 0.25 h on a standard laptop. Furthermore, we generate a phase diagram of SDE transformation under varying area differences, which further emphasizes the model's accuracy and computational efficiency. This work contributes to a deep learning approach for predicting RBC morphology transformations, offering a computationally efficient and accurate alternative to traditional methods. The model's ability to reproduce RBC morphology by controlling geometric features holds significant implications for understanding and diagnosing blood disorders.

Red blood cells (RBCs) are not merely microscopic entities circulating in our bloodstream; they are essential players in maintaining the delicate balance required for human health.[1] Their unique and specialized shapes, a biconcave disk structure, is intricately linked to their primary function, oxygen transport.[2] Abnormalities or variations in their morphology may serve as crucial diagnostic indicators for various health conditions, such as anemias, hemoglobin disorders, or other hematological disorders.[3–7] Thus, it is significant to understand the RBC morphology for clinicians in diagnosing and monitoring patients with blood-related disorders.

RBCs can exhibit a variety of shapes, as shown in Fig. 1, and their morphology is influenced by various factors. Mature and healthy RBCs have a biconcave discoid [Fig. 1(a)], characterized by a flattened, disk-like structure with a central concavity on both sides.[8] However, under certain conditions, they can take on different shapes.[9–11] For example, in conditions like hereditary spherocytosis,[11] RBCs lose their biconcave shape and become more spherical, known as spherocytes [Fig. 1(b)]. They are sometimes observed during the end stage of

RBCs, and may be targeted for removal by the spleen.[3,12] In sickle cell anemia,[13] RBCs can assume a crescent or sickle shape [Fig. 1(c)], affecting their ability to flow smoothly through blood vessels and leading to vaso-occlusive crisis. Moreover, some RBCs may exhibit a mouth-like or slit-like central area, known as stomatocytes [Fig. 1(d)], and such a shape abnormality is associated with various conditions, including hereditary stomatocytosis.[14] Some RBCs may adopt a spiked or burr-like appearance, known as echinocytes [Fig. 1(e)], characterized by the presence of numerous small, evenly spaced, and regularly blunt projections on their membrane.[15,16] The formation of echinocytes can be influenced by various factors,[16,17] including changes in osmotic conditions, alterations in pH, and certain diseases or metabolic disorders, such as renal and liver diseases due to changes in electrolyte balance and uremia. A similar shape to echinocyte is acanthocyte [Fig. 1(f)], with long, irregular, spiny uneven projections on the their membrane, often associated with certain medical conditions,[18,19] particularly those affecting lipid metabolism and the structure of cell membranes, such as neuroacanthocytosis syndromes.[20]
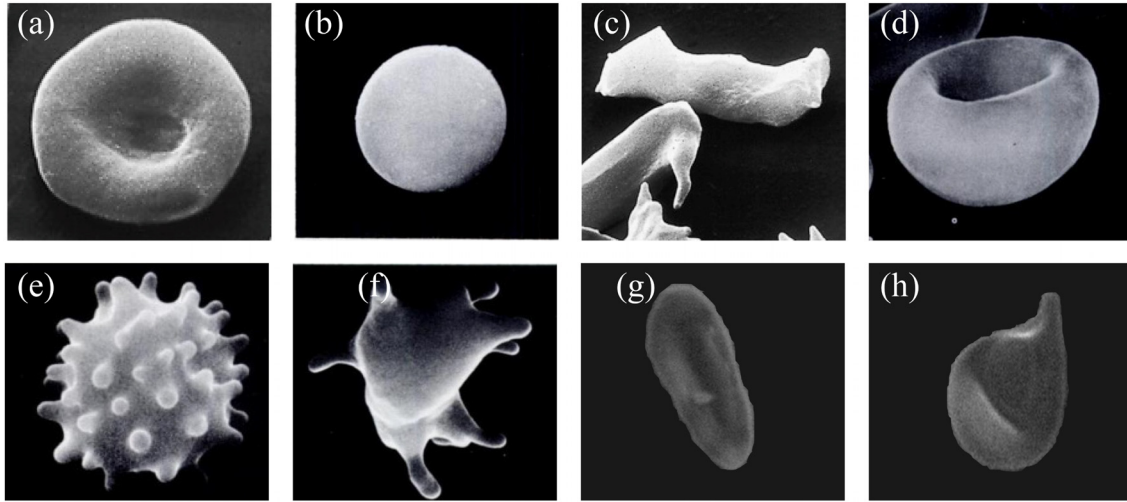
FIG. 1. RBC morphology observed using a scanning electron microscope: (a) discocyte,[10] (b) spherocyte,[10] (c) sickle,[10] (d) stomatocyte,[10] (e) echinocyte,[10] (f) acanthocyte,[10] (g) elliptocyte,[7] (h) dacrocyte.[7] (a)–(f) Reproduced with permission from Bain *et al.*, *Dacie and Lewis Practical Hematology*, 12th ed. (Elsevier, 2017). Copyright 2017 Elsevier.[10] (g) and (h) Reproduced with permission from J. Clin. Pathol. **72**, 520–524 (2019). Copyright 2019 BMJ Publishing Group.[7]

Apart from those, RBCs may exhibit an elliptical or oval shape [known as elliptocyte or ovalocyte, Fig. 1(g)] seen in conditions like elliptocytosis,[21] and a teardrop or pear shape [known as dacrocytes, Fig. 1(h)] found primarily in diseases with bone marrow fibrosis, such as myelofibrosis and myelophthisis caused by metastatic cancers.[22]

Previous studies indicate that the variations in RBC morphology are closely linked to their geometric properties, e.g., surface area, volume, and curvature.[23] For example, RBCs undergo distinct shape changes during aging, which are strongly associated with a reduction in surface area.[24,25] Another notable example is the stomatocyte–discocyte–echinocyte (SDE) transformation.[26] Stomatocytes exhibit cup-like concave shapes, while echinocytes have crenated and spiculated surfaces. These shapes are further categorized into four subclasses (I to IV) based on different levels of concavity and crenation. Sheetz and Singer proposed the bilayer-couple hypothesis to explain SDE transformation, suggesting that the two leaflets of membrane bilayer respond differently to various conditions.[27] When the outer leaflet expands relative to the inner leaflet, convex shapes form on the membrane surface, resulting in echinocytes. Conversely, when the inner leaflet expands relative to the outer leaflet, concave shapes form, producing stomatocytes. Consequently, the bilayer-couple hypothesis provides an explanation for the universal nature of SDE transformation, asserting that alterations in the relaxed area difference between leaflets are both necessary and sufficient to induce shape transitions.

There are two basic approaches for modeling cell deformation: continuum and discrete models.[28,29] Continuum models treat the cell as a continuous material, and employ constitutive equations, such as the neo-Hookean (NH)[30] and Skalak (SK) laws,[31] to describe the stress–strain relationships.[32–36] Discrete models, such as particle-based approaches, represent the cell membrane as a collection of interconnected particles or elements.[37–40] They often incorporate the microstructure of the membrane, offering deeper insights into the local deformations and structural changes.[41,42] In the present work, we aim to develop a deep neural network (DNN) model to quickly reproduce

the RBC morphology by controlling the geometric properties, with the dataset generated by a discrete model. The geometric properties feed into a deep neural network, yielding the RBC shape as the output. Thus, a correspondence between cell shape and its geometric properties is established based on a discrete model of cell deformation.

In our previous work,[43] we utilized a discrete model to obtain the RBC equilibrium shapes for given geometric properties, generating a dataset for the present DNN model. In the discrete model, particles are distributed on a membrane to represent actin junctional complexes, and the connection between two particles represents a cytoskeletal spectrin link. All connections form a two-dimensional triangle network, representing the cell membrane. Each particle follows specific physical laws, for example, the Newton's second law to obtain the RBC shape at equilibrium,[36]

$$\begin{cases} m\dfrac{\mathrm{d}^2\boldsymbol{x}_i}{\mathrm{d}t^2} + \mu\dfrac{\mathrm{d}\boldsymbol{x}_i}{\mathrm{d}t} = \boldsymbol{F}_i, \\ \boldsymbol{x}_i(0) = \boldsymbol{x}_i^0, \\ \boldsymbol{v}_i(0) = \boldsymbol{v}_i^0, \end{cases} \quad (1)$$

where t is the time, m and $\boldsymbol{x}_i$ are the mass and position of particle i, μ is the membrane viscosity, $\boldsymbol{F}_i$ is the nodal force due to the cell deformation, and $\boldsymbol{x}_i^0$ and $\boldsymbol{v}_i^0$ are the initial conditions. To describe the cell deformation, a total free energy is associated with the triangular network, consisting of the in-plane (U_s), bending (U_b), area-constraint (U_a), volume constraint (U_v), and area difference (U_{ad}) energies,[44]

$$U = U_s + U_b + U_a + U_v + U_{ad}, \quad (2)$$

such that

$$\boldsymbol{F}_i = -\frac{\partial U}{\partial \boldsymbol{x}_i}. \quad (3)$$

The detailed formulations of these energies can be found in Refs. 27 and 43–52. The discrete models start from initial conditions with $\boldsymbol{x}_i^0$

and v_i^0, for example, a sphere initial configuration and zero initial velocity, to find an equilibrium state under several given geometric properties, by minimizing the total free energy. These properties include the global properties—surface area A_0, volume V_0, direction-dependent area difference ΔA_0, and direction-independent area difference $\Delta A_0'$, and the local averaged properties—spring length l_0, triangle area a_0 and edge curvature m_0.

The present DNN model aims to find an equilibrium state, which is an inverse problem to determine the function

$$\boldsymbol{x} = \boldsymbol{g}(\boldsymbol{y}), \tag{4}$$

for given initial conditions of $\boldsymbol{x}_i^0$ and $\boldsymbol{v}_i^0$, where

$$\boldsymbol{x} = (\boldsymbol{x}_1, \boldsymbol{x}_2, ..., \boldsymbol{x}_{N_v}), \tag{5}$$

$$\boldsymbol{y} = (A_0, V_0, \Delta A_0, \Delta A_0', l_0, a_0, m_0). \tag{6}$$

The corresponding forward problem is to calculate the geometric properties when the RBC shape is given, expressed as

$$\boldsymbol{y} = \boldsymbol{h}(\boldsymbol{x}). \tag{7}$$

The forward problem is well-posed, yielding a unique solution $\boldsymbol{y}$ for a given $\boldsymbol{x}$. That is, the geometric properties can be uniquely determined for a given cell shape. On the contrary, the inverse problem is mostly ill-posed, and it may have a large number of solutions $\boldsymbol{x}$ for a given $\boldsymbol{y}$.

Algorithm 1: Dataset construction.

Data: Input times N_I
Result: Dataset D_S

1 /* initialize an input   */
2 Give Set initial value $\boldsymbol{y} = (A_0, V_0, \Delta A_0, \Delta A_0', l_0, a_0, m_0)$;
3 **for** $n \leq N_I$ **do**
4   /* initialize the particle system   */
5   Initialize $\boldsymbol{x}$ with a sphere of A_0 and V_0;
6   Set m, μ, Δt;
7   Set tol;   // tol is an error tolerance
8   /* update the particle system   */
9    $k \leftarrow 0$;   // k is the current time step
10   **do**
11   **for** $i \leq N_v$ **do**
12   Calculate the force $\boldsymbol{F}_i$;
13   Solve $\boldsymbol{x}_i$ by Runge-Kutta method;
14   **end**
15   Calculate the geometric properties $\boldsymbol{y}$;
16   Add $(\boldsymbol{y}, \boldsymbol{x})$ into D_S;   // D_S is the dataset
17     $k = k + 1$;   // update the time step
18     $\varepsilon = \max|\boldsymbol{F}_i|$;   //$\varepsilon$ is the current error
19   **while** $\varepsilon < tol$;
20   /* adjust the current input as a new one   */
21   Make an adjustment to $\boldsymbol{y}$;
22 **end**
23 /* Output the dataset   */
24 Output the dataset D_S;

To reduce the degree of freedom of $\boldsymbol{x}$, we reconstruct the membrane surface with spherical harmonics, which requires a one-to-one mapping between Cartesian and spherical coordinates, $\boldsymbol{x} = (x(\theta, \varphi), y(\theta, \varphi), z(\theta, \varphi))$ with $\phi \in [0, \pi]$ and $\theta \in [0, 2\pi]$, called surface parameterization. Therefore, the full coordinate function of any point on the membrane surface can be expressed as an expansion of the spherical harmonic series,[53–55]

$$\begin{cases} x(\theta, \varphi) = \sum_{n=0}^{\infty} \sum_{m=-n}^{n} c_{xn}^m Y_n^m(\theta, \varphi), \\ y(\theta, \varphi) = \sum_{n=0}^{\infty} \sum_{m=-n}^{n} c_{yn}^m Y_n^m(\theta, \varphi), \\ z(\theta, \varphi) = \sum_{n=0}^{\infty} \sum_{m=-n}^{n} c_{zn}^m Y_n^m(\theta, \varphi), \end{cases} \tag{8}$$

where c_{xn}^m, c_{yn}^m, and c_{zn}^m are spherical harmonic coefficients, and $Y_n^m(\theta, \varphi)$ is the spherical harmonic function given by

$$Y_n^m(\theta, \varphi) = \sqrt{\frac{(2n+1)(n-m)!}{4\pi(n+m)!}} P_n^m(\cos\theta) e^{im\varphi}, \tag{9}$$

and $P_n^m(x)$ is the associated Legendre function. The index n is truncated up to $\bar{n}$ in simulations, and $\bar{n} = 15$ is reported to be enough for most engineering applications.[55,56] There are totally $3(\bar{n}+1)^2$ coefficients to be determined in Eq. (8),

$$\boldsymbol{c} = \begin{pmatrix} c_{x0}^0 & c_{x1}^{-1} & c_{x1}^0 & c_{x1}^1 & \cdots & c_{x\bar{n}}^{\bar{n}} \\ c_{y0}^0 & c_{y1}^{-1} & c_{y1}^0 & c_{y1}^1 & \cdots & c_{y\bar{n}}^{\bar{n}} \\ c_{z0}^0 & c_{z1}^{-1} & c_{z1}^0 & c_{z1}^1 & \cdots & c_{z\bar{n}}^{\bar{n}} \end{pmatrix}, \tag{10}$$

which is significantly smaller than the degree of freedom of $\boldsymbol{x}$, $3N_v$. For example, representing a smooth RBC surface using particles would require 2500 particles, resulting in 7500 degrees of freedom across three spatial directions. The spherical harmonics has only 768 coefficients with $\bar{n} = 15$ to adequately represent a smooth surface, significantly reducing the degrees of freedom. Eq. (8) can be rewritten in a form of matrix as

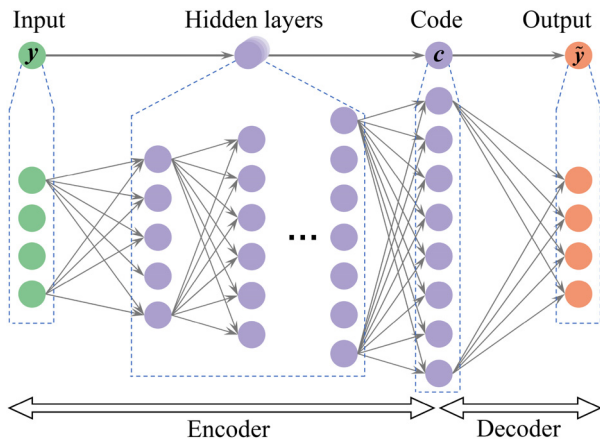$$\boldsymbol{x} = \boldsymbol{c}Y, \tag{11}$$

where

$$\boldsymbol{Y} = \begin{pmatrix} Y_0^0(\theta_1, \varphi_1) & Y_0^0(\theta_2, \varphi_2) & \cdots & Y_0^0(\theta_{N_v}, \varphi_{N_v}) \\ Y_1^{-1}(\theta_1, \varphi_1) & Y_1^{-1}(\theta_2, \varphi_2) & \cdots & Y_1^{-1}(\theta_{N_v}, \varphi_{N_v}) \\ Y_1^0(\theta_1, \varphi_1) & Y_1^0(\theta_2, \varphi_2) & \cdots & Y_1^0(\theta_{N_v}, \varphi_{N_v}) \\ Y_1^1(\theta_1, \varphi_1) & Y_1^1(\theta_2, \varphi_2) & & \\ \vdots & \vdots & \vdots & \vdots \\ Y_{\bar{n}}^{\bar{n}}(\theta_1, \varphi_1) & Y_{\bar{n}}^{\bar{n}}(\theta_2, \varphi_2) & \cdots & Y_{\bar{n}}^{\bar{n}}(\theta_{N_v}, \varphi_{N_v}) \end{pmatrix}, \tag{12}$$

and (θ_i, φ_i) are the ith pair of the spherical coordinates of the particle $\boldsymbol{x}_i = (x_i, y_i, z_i)$. Correspondingly, Eq. (4) is transformed into

$$\boldsymbol{c} = \tilde{\boldsymbol{g}}(\boldsymbol{y}), \tag{13}$$

and Eq. (7) is modified to

FIG. 2. The fully connected structure of deep neural network with an overcomplete encoder and undercomplete decoder, where $\tilde{y}$ is the predicted geometric property.

$$y = \tilde{h}(c). \tag{14}$$

We develop a deep neural network (DNN), as shown in Fig. 2, to solve the inverse problem (13). It is similar to an overcomplete autoencoder with an encoder and a decoder. The encoder is overcomplete and designed to determine Eq. (13), with multiple fully connected hidden layers. The decoder is used to determine Eq. (14), which can be explicitly formulated without requiring DNN. The loss function is defined by

$$L = \overbrace{|c - \tilde{c}|^2}^{\text{harmonic coefficients}} + \overbrace{\lambda|y - \tilde{y}|^2}^{\text{geometric properties}}, \tag{15}$$

where c represents the training data obtained by solving Eq. (11) and y is the corresponding geometric data, $\tilde{c}$ represents the predicted results obtained by DNN and $\tilde{y}$ is the corresponding geometric property, and $\lambda \in [0, 1]$ is a parameter to control the importance of the geometric loss. It is still challenging to find the desired solution for the optimization problem in Eq. (15) with the designed DNN due to the notable mismatch in dimensions. The input dimension, denoted as $\dim(y) = 7$, remains smaller than the code dimension with $\dim(c) = 3(\bar{n} + 1)^2$. In such a circumstance, whether the desired solution is obtained depends on the quality and quantity of data. For this purpose, we construct a sufficiently large and diverse dataset by solving Eq. (1),[43] which is used to train the DNN and narrow down the solution range. A Runge–Kutta method is here considered to solve Eq. (1), and Algorithm 1 illustrates a procedure to construct the dataset.

The DNN model is employed to predict the complete sequence of stomatocyte–discocyte–echinocyte (SDE) transformation of a RBC. Figure 3 shows a comparison of SDE transformation among the experimental observations,[14] numerical simulations,[43] and the present DNN
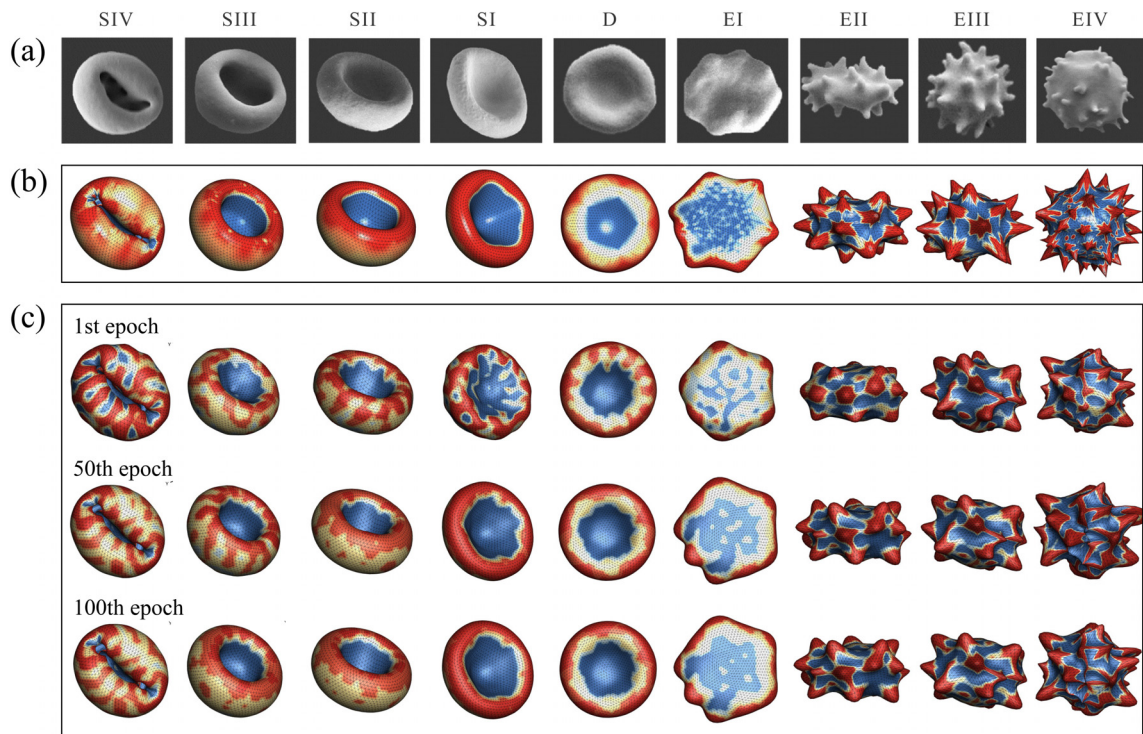
FIG. 3. Comparisons of SDE transformation among (a) experimental observations,[14] (b) numerical simulations,[43] and (c) DNN predictions at different training epochs, where the symbol "S" at the top denotes stomatocyte, "D" denotes discocyte, and "E" denotes echinocyte. (a) Reproduced with permission from Geekiyanage *et al.*, PLoS One 14, e0215447 (2019). Copyright 2019 Authors, licensed under a Creative Commons Attribution (CC BY) license.[14] (b) Reproduced with permission Tan, J. Appl. Phys. 136, 214702 (2024). Copyright 2024 AIP Publishing.[43]
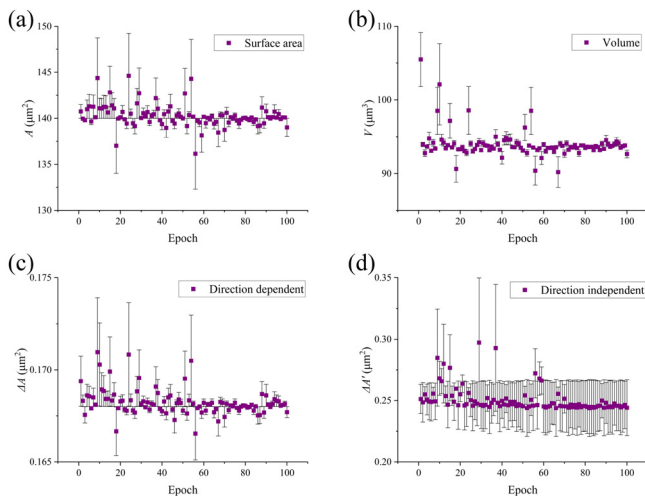
TABLE I. The direction-dependent and independent area differences of each SDE shape of RBC.

Shape	SIV	SIII	SII	SI	D	EI	EII	EIII	EIV
ΔA	0.07	0.14	0.147	0.161	0.168	0.189	0.266	0.315	0.42
$\Delta A'$	0.42	0.273	0.245	0.231	0.259	0.28	0.77	0.84	1.26

predictions. Each RBC shape has identical properties—$A_0 = 140\,\mu m^2$, $V_0 = 93.48\,\mu m^3$, $l_0 = 0.254\,\mu m$, $a_0 = 0.0273\,\mu m$, and $m_0 = 0.0056\,\mu m$, but different area differences ΔA and $\Delta A'$ detailed in Table I. The results indicate that the DNN model can accurately predict the complete sequence of the SDE transformation, with a loss magnitude on the order of 10^{-5}, closely aligning with both experimental observations and numerical simulations. This highlights the potential of the DNN model to reproduce RBC morphology by controlling geometric features. Additionally, two phenomena are observed from the comparison. First, the RBC surface is less smooth at small training epochs, but gradually becomes smoother as the epoch increases, as seen in stages SI and SIV. This suggests that the training quality improves with increase in the training epoch. Figure 4 illustrates the variations of four global geometric properties during the training process, which approach their respective steady-state values. Second, the echinocyte spicules in the DNN model are less sharp than those in the experimental and numerical results. This discrepancy arises because the RBC shape is represented by a series of spherical harmonics. As the number $\bar{n}$ of spherical harmonics is increased, the spicules become more similar to those in the experimental and numerical results. For example, the spicules at $\bar{n} = 25$ are obviously sharper than that at $\bar{n} = 10$, and there are no spicules at $\bar{n} < 5$, as shown in Fig. 5.

To evaluate the performance of our DNN model, we examine the effects of DNN structural parameters, including dataset size and hidden layer number. When the dataset size is 89, the cell surface appears less smooth; however, it becomes smoother when the dataset size
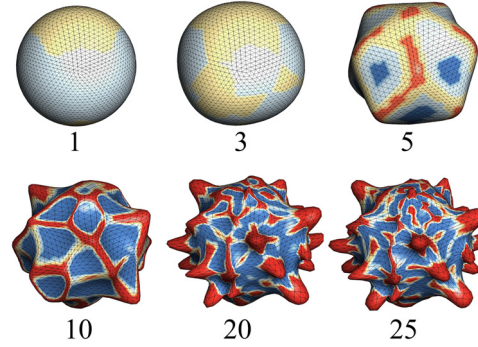
FIG. 5. The EIV shape at different number $\bar{n}$ of spherical harmonics.

exceeds 170, as shown in Fig. 6(a). This suggests that even a small dataset can accurately generate the discocyte RBC morphology. It should be noted that the training process takes only about 1h CPU time at a dataset size of 170 but 7 h at a dataset size of 1780, where the number of hidden layers is fixed at 12. Figure 6(c) illustrates the loss variation $|c - \tilde{c}|$ with respect to the dataset size, showing a decreasing trend as expected.

We increase the number of the hidden layers from 6 to 14, and find that the results did not exhibit significant changes, as shown in Fig. 6(b). This implies that our DNN model is capable of accurately predicting cell shapes without requiring an excessive number of hidden layers. Note that the CPU time increases dramatically from 3 to 18 h when the number of hidden layers is increased from 6 to 14, where the dataset size is fixed at 1780. Moreover, the loss of $|c - \tilde{c}|$ does not monotonically decrease with increase in the layer number, but instead remains on the order of 10^{-5}, as shown in Fig. 6(d). When the dataset size is 170 and the number of hidden layers is 6, the simulation results are highly consistent with the target cell morphology at the epoch of 100, as shown in Fig. 6(e). In such a case, the CPU time is only 0.25 h, demonstrating the model's robustness and efficiency. To further evaluate the prediction accuracy, a fivefold cross-validation is carried out at this minimum model size. All the predicted shapes are almost similar with a mean loss of 3.47×10^{-5}. Figure 6(f) shows five predicted shapes from the cross-validation.
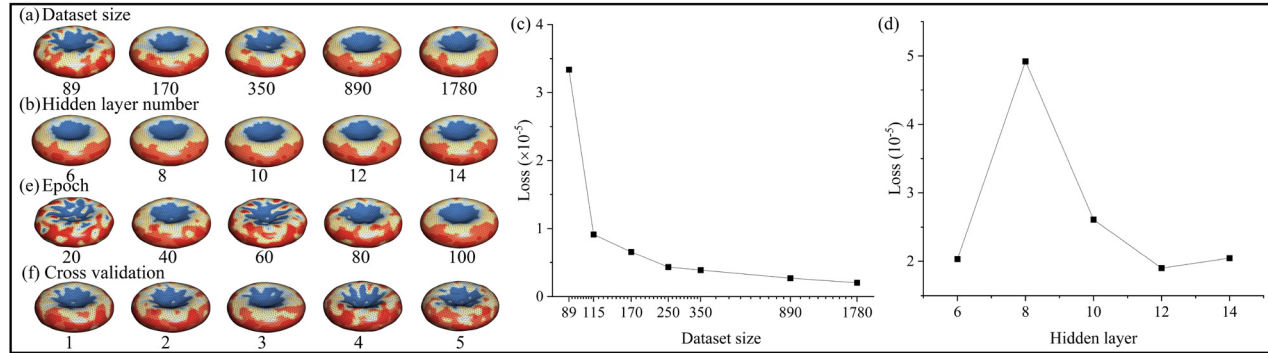
We employed our DNN model to investigate the phase diagram of SDE transformation under varying direction-dependent and independent area differences, as depicted in Fig. 7. By decomposing ΔA into two positive components,

$$\Delta A = \Delta A^+ - \Delta A^-, \qquad (16)$$

where $\Delta A^+ > 0$ and $\Delta A^- > 0$, $\Delta A'$ can be expressed as

$$\Delta A' = \Delta A^+ + \Delta A^-. \qquad (17)$$

When ΔA^- is large, implying that ΔA is small while $\Delta A'$ is large, the cell invagination becomes so severe that the invaginated parts overlap. This condition exhibits an invalid state, labeled as 0 in the upper-left region of Fig. 7. When ΔA^- is not too large, the cell state largely depends on ΔA^+. The cell is found to exhibit SIV stages if $\Delta A^+ \approx 2\Delta A^-$, i.e., $\Delta A' \approx 3\Delta A$, which corresponds to the diagonal region in Fig. 7, labeled as 1. If $\Delta A^+ > 2\Delta A^-$, the cell surface protrudes, forming spicules. Moreover, as ΔA^+ increases, i.e., as both ΔA

FIG. 4. The variations of (a) surface area A, (b) volume V, (c) direction-dependent area difference ΔA, and (d) direction-independent area difference $\Delta A'$ with respect to the training epoch when predicting discocyte RBC.

FIG. 6. Effects of DNN structure on the prediction of discocyte RBC: (a) discocyte shapes for different dataset sizes, (b) discocyte shapes for different numbers of hidden layers, (c) loss of $|c - \tilde{c}|$ for different dataset sizes, (d) loss of $|c - \tilde{c}|$ for different numbers of hidden layers, (e) discocyte shapes under different training epochs for a dataset size of 170 and hidden layer number of 6, serving as the minimal model, and (f) discocyte shapes under fivefold cross-validation of the minimal model.
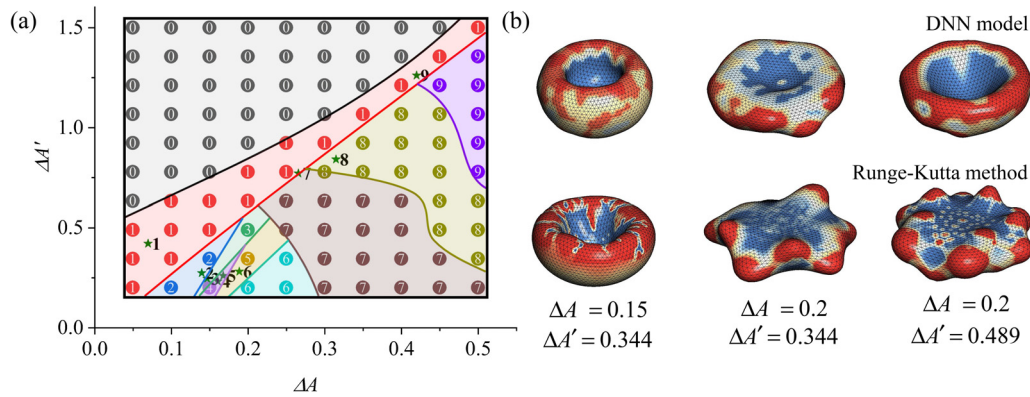
FIG. 7. (a) Phase diagram of SDE transformation under varying ΔA and $\Delta A'$, and (b) three different states predicted by the DNN model and Runge–Kutta method. The numbers denote the different stages of SDE. The numbers from 1 to 9 correspond sequentially to SIV to EIV, while the number 0 represents an invalid state with the overlapping invaginated part. The points marked with stars correspond to the results presented in Fig. 3.

and $\Delta A'$ become larger, the spicules become more pronounced. This condition exhibits an echinocyte stage, corresponding to the regions labeled as 7–9. When $\Delta A^+ < 2\Delta A^-$, the cell exhibits invagination, with the degree of invagination becoming more pronounced as ΔA^+ decreases. For example, when ΔA^+ is slightly smaller than $2\Delta A^-$, the invagination occurs on one side of the cell, exhibiting the stomatocyte states labeled as 2–4. When ΔA^+ is much smaller than $2\Delta A^-$, the invagination appears on both sides of the cell, exhibiting the discocyte state labeled as 5. In fact, the values of ΔA and $\Delta A'$ change within 0.05 for the states from EI to SIII, as shown in Table I. This suggests that these five states (labeled as 2–6) are highly sensitive to changes in ΔA and $\Delta A'$, making it challenging to precisely identify their phase regions. The sensitivity is further confirmed by comparing the phase diagram predicted by the DNN and that obtained by solving Eq. (1) with the Runge–Kutta method. They are in good agreement for the equilibrium states labeled by 0, 1, and 7–9. However, three states are not correctly predicted: the states at $\Delta A = 0.15$ and $\Delta A' = 0.344$, $\Delta A = 0.2$ and $\Delta A' = 0.344$, and $\Delta A = 0.2$ and $\Delta A' = 0.489$, as shown in Fig. 7(b). For example, at $\Delta A = 0.15$ and $\Delta A' = 0.344$, the DNN predicts a SIII state with the label 2, while the mechanical model gives a SII state with the label 3.

It is highlighted that the phase diagram is generated by predicting 100 shapes from a dataset comprising 4000 entries, requiring 32 h of CPU time. If we directly solve Eq. (1) using the Runge–Kutta method, getting each shape requires on average 24 h, resulting in 2400 h for 100 shapes.[43] Thus, the DNN model is 125 times more efficient than the direct method. More importantly, once adequately trained, the DNN model requires no additional CPU time for new inputs. Consequently, predicting a single shape is computationally equivalent to predicting 10 000 shapes, a task infeasible for direct methods.

We developed a deep learning model to predict the RBC morphological transformations with high accuracy and efficiency. The model integrates a traditional discrete model for dataset generation and spherical harmonics for RBC surface reconstruction, thereby reducing computational complexity while maintaining precision. A deep learning architecture, combining an autoencoder and fully connected neural network, was designed to solve the inverse problem of inferring RBC shapes from geometric properties. Therefore, the model performance primarily depends on the dataset quality, spherical harmonic reconstruction, and network architecture.

The deep learning model was used to predict the stomatocyte–discocyte–echinocyte transformation, and the results align closely with

experimental observations and numerical simulations, validating its accuracy. The model also exhibits low sensitivity to dataset size and hidden layer depth, remaining effective even when using a small dataset and shallow hidden layers, thereby demonstrating robustness. This is particularly beneficial in scenarios where computational resources are limited. However, the number of spherical harmonic functions significantly influences model predictions. Prior studies have reported that 15 functions are sufficient for most engineering applications.[55,56] Insufficient functions hinder accurate shape reconstruction, whereas excessive functions increase computational complexity. Furthermore, the model was used to generate a phase diagram of stomatocyte–discocyte–echinocyte transformation under varying area differences. This study not only provides valuable insights into the morphological changes of RBCs, but also highlights the model's accuracy and efficiency.

While the DNN model provides an accurate and efficient alternative to traditional methods for reproducing RBC morphology, two primary limitations must be highlighted. First, the model's performance depends on the training dataset, and only SDE dataset is used in the present work. Hence, generalizing to pathological or highly irregular RBC shapes would require new datasets capturing specific morphological variations. Second, although seven geometric features in this study can effectively characterize shape changes during SDE transitions, they may fail to resolve other RBC shapes. Identifying more geometric features is essential, particularly those capturing localized shape variations. Additionally, experimental measurement of area differences poses challenges, and thus it would be more feasible and clinically relevant to extend them to other factors, such as pH, osmotic conditions, or even disease states. Therefore, future work should focus on exploring the model's applications in complex biological systems and clinical settings, e.g., 3D reconstruction of cell morphology, by constructing a comprehensive dataset that integrates experimental or clinical data.

AUTHOR DECLARATIONS
Conflict of Interest

The author has no conflicts to disclose.

Author Contributions

Sisi Tan: Conceptualization (equal); Data curation (lead); Formal analysis (lead); Investigation (lead); Methodology (lead); Validation (lead); Visualization (lead); Writing – original draft (lead); Writing – review & editing (lead).

DATA AVAILABILITY

The data that support the findings of this study are available from the corresponding author upon reasonable request.

REFERENCES

[1]N. Mohandas and P. G. Gallagher, "Red cell membrane: Past, present, and future," Blood **112**, 3939–3948 (2008).

[2]B. J. Bain, "Structure and function of red and white blood cells and platelets," Medicine **49**, 183–188 (2021).

[3]B. Blasi, A. D'alessandro, N. Ramundo, and L. Zolla, "Red blood cell storage and cell morphology," Transfus. Med. **22**, 90–96 (2012).

[4]K. Jaferzadeh and I. Moon, "Quantitative investigation of red blood cell three-dimensional geometric and chemical changes in the storage lesion using digital holographic microscopy," J. Biomed. Opt. **20**, 111218 (2015).

[5]X. Li, H. Li, H. Y. Chang, G. Lykotrafitis, and G. E. Karniadakis, "Computational biomechanics of human red blood cells in hematological disorders," J. Biomech. Eng. **139**, 0210081 (2017).

[6]H. Li, L. Lu, X. Li, P. A. Buffet, M. Dao, G. E. Karniadakis, and S. Suresh, "Mechanics of diseased red blood cells in human spleen and consequences for hereditary blood disorders," Proc. Natl. Acad. Sci. U. S. A. **115**, 9574–9579 (2018).

[7]P. Chaichompoo, A. Qillah, P. Sirankapracha, J. Kaewchuchuen, P. Rimthong, K. Paiboonsukwong, S. Fucharoen, S. Svasti, and S. Worawichawong, "Abnormal red blood cell morphological changes in thalassaemia associated with iron overload and oxidative stress," J. Clin. Pathol. **72**, 520–524 (2019).

[8]L. Mesarec, M. Drab, S. Penič, V. Kralj-Iglič, and A. Iglič, "On the role of curved membrane nanodomains and passive and active skeleton forces in the determination of cell shape and membrane budding," Int. J. Mol. Sci. **22**, 2348 (2021).

[9]S. V. Rudenko, "Erythrocyte morphological states, phases, transitions and trajectories," Biochim. Biophys. Acta. **1798**, 1767–1778 (2010).

[10]B. J. Bain, I. Bates, and M. A. Laffan, "Chapter 5: Blood cell morphology in health and disease," *Dacie and Lewis Practical Haematology*, 12th ed. (Elsevier, 2017), pp. 61–92.

[11]J. Sikdar, P. Seal, A. Roy, and R. Haldar, "Cigarette smokers develop altered erythrocyte membrane composition: An investigation unmasking the role of membrane bound integral protein glut 1," Free Radical. Res. **51**, 375–388 (2017).

[12]S. M. Frank, B. Abazyan, M. Ono, C. W. Hogue, D. B. Cohen, D. E. Berkowitz, P. M. Ness, and V. M. Barodka, "Decreased erythrocyte deformability after transfusion and the effects of erythrocyte storage duration," Anesth. Analg. **116**, 975 (2013).

[13]A. Abay, G. Simionato, R. Chachanidze, A. Bogdanova, L. Hertz, P. Bianchi, E. Van den Akker, M. von Lindern, M. Leonetti, G. Minetti *et al.*, "Glutaraldehyde—A subtle tool in the investigation of healthy and pathologic red blood cells," Front. Phys. **10**, 514 (2019).

[14]N. M. Geekiyanage, M. A. Balanant, E. Sauret, S. Saha, R. Flower, C. T. Lim, and Y. Gu, "A coarse-grained red blood cell membrane model to study stomatocyte-discocyte-echinocyte morphologies," PLoS One **14**, e0215447 (2019).

[15]R. Mukhopadhyay, H. W. G. Lim, and M. Wortis, "Echinocyte shapes: Bending, stretching, and shear determine spicule shape and spacing," Biophys. J. **82**, 1756–1772 (2002).

[16]K. D. Tachev, K. D. Danov, and P. A. Kralchevsky, "On the mechanism of stomatocyte–echinocyte transformations of red blood cells: Experiment and theoretical model," Colloids Surf., B **34**, 123–140 (2004).

[17]H. W. G. Lim, M. Wortis, and R. Mukhopadhyay, "Stomatocyte–discocyte–echinocyte sequence of the human red blood cell: Evidence for the bilayer–couple hypothesis from membrane mechanics," Proc. Natl. Acad. Sci. U. S. A. **99**, 16766–16769 (2002).

[18]A. Foglia, "The acanthocyte-echinocyte differential," Swiss Med. Wkly. **140**, 1–3 (2010).

[19]Z. X. Tong, X. Chen, Y. L. He, and X. B. Liao, "Coarse-grained area-difference-elasticity membrane model coupled with IB–LB method for simulation of red blood cell morphology," Physica A **509**, 1183–1194 (2018).

[20]J. C. A. Cluitmans, C. Tomelleri, Z. Yapici, S. Dinkla, P. Bovee-Geurts, V. Chokkalingam, L. De Franceschi, R. Brock, and G. J. G. C. M. Bosman, "Abnormal red blood cell structure and function in neuroacanthocytosis," PLoS One **10**, e0125580 (2015).

[21]R. Jindal and S. Batoye, "SEM studies on erythrocyte alterations in ctenopharyngodon idellus (cuvier and valenciennes) induced by fenvalerate," Res. J. Anim. Vet. Fish. Sci. **3**, 1–5 (2015).

[22]I. Gütgemann, H. Heimpel, and C. T. Nebe, "Significance of teardrop cells in peripheral blood smears," Laboratoriumsmedizin **38**, 000010151520140005 (2014).

[23]L. Mesarec, W. Góźdź, A. Iglič, V. Kralj-Iglič, E. G. Virga, and S. Kralj, "Normal red blood cells' shape stabilized by membrane's in-plane ordering," Sci. Rep. **9**, 19742 (2019).

[24]R. E. Waugh, M. Narla, C. W. Jackson, T. J. Mueller, T. Suzuki, and G. L. Dale, "Rheologic properties of senescent erythrocytes: Loss of surface area and volume with red blood cell age," Blood **79**, 1351–1358 (1992).

[25]Q. Wei, X. Wang, C. Zhang, M. Dao, and X. Gong, "Evolution of surface area and membrane shear modulus of matured human red blood cells during mechanical fatigue," Sci. Rep. **13**, 8563 (2023).

[26]H. W. G. Lim, "A numerical study of morphologies and morphological transformations of human erythrocyte based on membrane mechanics," Ph.D. thesis (Simon Fraser University, 2003).

[27]M. P. Sheetz and S. J. Singer, "Biological membranes as bilayer couples. A molecular mechanism of drug-erythrocyte interactions," Proc. Natl. Acad. Sci. U. S. A. **71**, 4457–4461 (1974).

[28]C. T. Lim, E. H. Zhou, and S. T. Quek, "Mechanical models for living cells—A review," J. Biomech. **39**, 195–216 (2006).

[29]X. Li, P. M. Vlahovska, and G. E. Karniadakis, "Continuum-and particle-based modeling of shapes and dynamics of red blood cells in health and disease," Soft Matter **9**, 28–37 (2013).

[30]X. Q. Hu, B. Sévénié, A. V. Salsac, E. Leclerc, and D. Barthès-Biesel, "Characterizing the membrane properties of capsules flowing in a square-section microfluidic channel: Effects of the membrane constitutive law," Phys. Rev. E **87**, 063008 (2013).

[31]R. Skalak, A. Tozeren, R. Zarda, and S. Chien, "Strain energy function of red blood cell membranes," Biophys. J. **13**, 245–264 (1973).

[32]D. Barthes-Biesel, A. Diaz, and E. Dhenin, "Effect of constitutive laws for two-dimensional membranes on flow-induced capsule deformation," J. Fluid Mech. **460**, 211–222 (2002).

[33]E. Lac, D. Barthes-Biesel, N. A. Pelekasis, and J. Tsamopoulos, "Spherical capsules in three-dimensional unbounded stokes flows: Effect of the membrane constitutive law and onset of buckling," J. Fluid Mech. **516**, 303–334 (2004).

[34]P. Dimitrakopoulos, "Analysis of the variation in the determination of the shear modulus of the erythrocyte membrane: Effects of the constitutive law and membrane modeling," Phys. Rev. E **85**, 041917 (2012).

[35]X. Q. Hu, A. V. Salsac, and D. Barthès-Biesel, "Flow of a spherical capsule in a pore with circular or square cross-section," J. Fluid Mech. **705**, 176–194 (2012).

[36]K-i Tsubota, "Short note on the bending models for a membrane in capsule mechanics: Comparison between continuum and discrete models," J. Comput. Phys. **277**, 320–328 (2014).

[37]I. V. Pivkin and G. E. Karniadakis, "Accurate coarse-grained modeling of red blood cells," Phys. Rev. Lett. **101**, 118105 (2008).

[38]D. A. Fedosov, B. Caswell, and G. E. Karniadakis, "Systematic coarse-graining of spectrin-level red blood cell models," Comput. Method Appl. Mech. Eng. **199**, 1937–1948 (2010).

[39]T. Ye, N. Phan-Thien, and C. T. Lim, "Particle-based simulations of red blood cells—A review," J. Biomech. **49**, 2255–2266 (2016).

[40]T. Ye, L. Peng, and G. Li, "Red blood cell distribution in a microvascular network with successive bifurcations," Biomech. Model. Mechanobiol. **18**, 1821–1839 (2019).

[41]W. B. Gratzer, "The red cell membrane and its cytoskeleton," Biochem. J. **198**, 1–8 (1981).

[42]S. Suetsugu, S. Kurisu, and T. Takenawa, "Dynamic shaping of cellular membranes by phospholipids and membrane-deforming proteins," Physiol. Rev. **94**, 1219–1248 (2014).

[43]S. Tan, "Nonlinear modeling for predicting red blood cell morphological transformations," J. Appl. Phys. **136**, 214702 (2024).

[44]G. Závodszky, B. Van Rooij, V. Azizi, and A. Hoekstra, "Cellular level *in-silico* modeling of blood rheology with an improved material model for red blood cells," Front. Physiol. **8**, 563 (2017).

[45]G. Gompper and D. M. Kroll, "Random surface discretizations and the renormalization of the bending rigidity," J. Phys. I **6**, 1305–1320 (1996).

[46]F. Jülicher, "The morphology of vesicles of higher topological genus: Conformal degeneracy and conformal modes," J. Phys. II **6**, 1797–1824 (1996).

[47]T. Ye, N. Phan-Thien, C. T. Lim, L. Peng, and H. Shi, "Hybrid smoothed dissipative particle dynamics and immersed boundary method for simulation of blood cells in flows," Phys. Rev. E **95**, 063314 (2017).

[48]A. Guckenberger and S. Gekle, "Theory and algorithms to compute Helfrich bending forces: A review," J. Phys. **29**, 203001 (2017).

[49]L. Xiao, J. Chu, C. Lin, K. Zhang, S. Chen, and L. Yang, "Simulation of a tumor cell flowing through a symmetric bifurcated microvessel," Biomech. Model. Mechanobiol. **22**, 297–308 (2023).

[50]L. Miao, U. Seifert, M. Wortis, and H.-G. Döbereiner, "Budding transitions of fluid-bilayer vesicles: The effect of area-difference elasticity," Phys. Rev. E **49**, 5389 (1994).

[51]M. Chen and F. J. Boyle, "An enhanced spring-particle model for red blood cell structural mechanics: Application to the stomatocyte–discocyte–echinocyte transformation," J. Biomech. Eng. **139**, 121009 (2017).

[52]X. Bian, S. Litvinov, and P. Koumoutsakos, "Bending models of lipid bilayer membranes: Spontaneous curvature and area-difference elasticity," Comput. Methods Appl. Mech. Eng. **359**, 112758 (2020).

[53]B. Zhou, J. Wang, and B. Zhao, "Micromorphology characterization and reconstruction of sand particles using micro x-ray tomography and spherical harmonics," Eng. Geol. **184**, 126–137 (2015).

[54]D. Wei, J. Wang, J. Nie, and B. Zhou, "Generation of realistic sand particles with fractal nature using an improved spherical harmonic analysis," Comput. Geotech. **104**, 1–12 (2018).

[55]D. Wei, B. Zhao, and Y. Gan, "Surface reconstruction with spherical harmonics and its application for single particle crushing simulations," J. Rock Mech. Geotech. Eng. **14**, 232–239 (2022).

[56]E. J. Garboczi, "Three-dimensional mathematical analysis of particle shape using X-ray tomography and spherical harmonics: Application to aggregates used in concrete," Cem. Concr. Res. **32**, 1621–1638 (2002).